Available online at www.sciencedirect.com
SCIENCE DIRECT®
Fusion Engineering and Design 72 (2004) 93–110
Fusion Engineering and Design
www.elsevier.com/locate/fusengdes

Studies of liquid-metal erosion and free surface flowing liquid lithium retention of helium at the University of Illinois

J.P. Allain[a,*], M. Nieto[b], M.D. Coventry[b], R. Stubbers[b], D.N. Ruzic[b,**]

[a] *Argonne National Laboratory, 9700 S Cass Ave, Argonne, IL 60439, USA*
[b] *University of Illinois, Urbana-Champaign, Urbana, IL, USA*

Available online 9 September 2004

Abstract

The erosion of liquid-metals from low-energy particle bombardment at 45° incidence has been measured for a combination of species and target materials in the ion-surface interaction experiment (IIAX) at the University of Illinois Urbana-Champaign. Measurements include bombardment of liquid Li, Sn–Li and Sn by H^+, D^+, He^+, and Li^+ particles at energies from 100 to 1000 eV and temperatures from 20 to 420 °C. Lithium sputtering near and just above the melting point shows little change compared to room temperature, solid-Li yields. When lithium is sputtered, about 2/3 of the sputtered flux is in the charged state. Temperature-dependent sputtering results show enhanced (up to an order-of-magnitude increase) sputter yields as the temperature of the sample is increased about a factor of two of the melting point for all liquid-metals studied (e.g., Li, Sn–Li, and Sn). The enhancement is explained by two mechanisms: near-surface binding of eroded atoms and the nature of the near-surface recoil energy and angular distribution as a function of temperature.

The Flowing Liquid Retention Experiment (FLIRE) measured particle transport by flowing liquid films when exposed to energetic particles. Measurements of retention coefficient were performed for helium ions implanted by an ion beam into flowing liquid lithium at 230 °C in the FLIRE facility. A linear dependence of the retention coefficient with implanted particle energy is found, given by the expression $R = (5.3 \pm 0.2) \times 10^{-3}\,\mathrm{keV}^{-1}$. The ion flux level did not have an effect for the flux level used in this work ($\sim 10^{13}\,\mathrm{cm}^{-2}\,\mathrm{s}^{-1}$) and square root dependence with velocity is also observed, which is in agreement with existing particle transport models.

Keywords: Plasma; Evaporation; FLIRE

1. Introduction

Liquid-metal experiments in the Plasma-Material Interaction group at the University of Illinois at Urbana-Champaign have been designed to address two important technological issues with the application of liquids

* Corresponding author. Tel.: +1 630 252 5184; fax: +1 630 252 3250.
E-mail addresses: allain@anl.gov (J.P. Allain), druzic@uiuc.edu (D.N. Ruzic)
** Co-corresponding author.

0920-3796/$ – see front matter © 2004 Published by Elsevier B.V.
doi:10.1016/j.fusengdes.2004.07.006

as plasma-facing components (PFCs) in fusion devices: surface erosion (sputtering and evaporation) and particle retention in flowing systems (e.g., helium or hydrogen retention in free surface flowing liquid lithium). The first part of this manuscript will summarize work in the ion-surface interaction experiment (IIAX) designed to measure sputtering and evaporation from liquid-metals under a variety of conditions. Work on liquid-metal sputtering measurements in other devices is rather scarce and limited [1–5]. Most of the recent work on liquid-metal sputtering has been carried out at the PISCES-B linear plasma device at the University of San Diego at California and is included in a separate paper in this issue. The second part of this manuscript will summarize work in the flowing liquid surface retention experiment (FLIRE). FLIRE is designed to study the retention and transport of implanted helium and hydrogen ions in free surface flowing liquids, in particular: liquid lithium. This section will focus only on helium retention work done at the University of Illinois since no other facility is currently working in this area.

2. Liquid-metal erosion measurements in the ion-surface interaction experiment (IIAX)

The IIAX measures the absolute, angular resolved and self-sputtering yields of many particle/target combinations (Fig. 1). Complete details of the experimental system and its components can be found in earlier papers [6–11]. This section gives a brief description of the major components and systems followed by results of sputtering measurements from lithium, tin–lithium and tin, all in the liquid state.

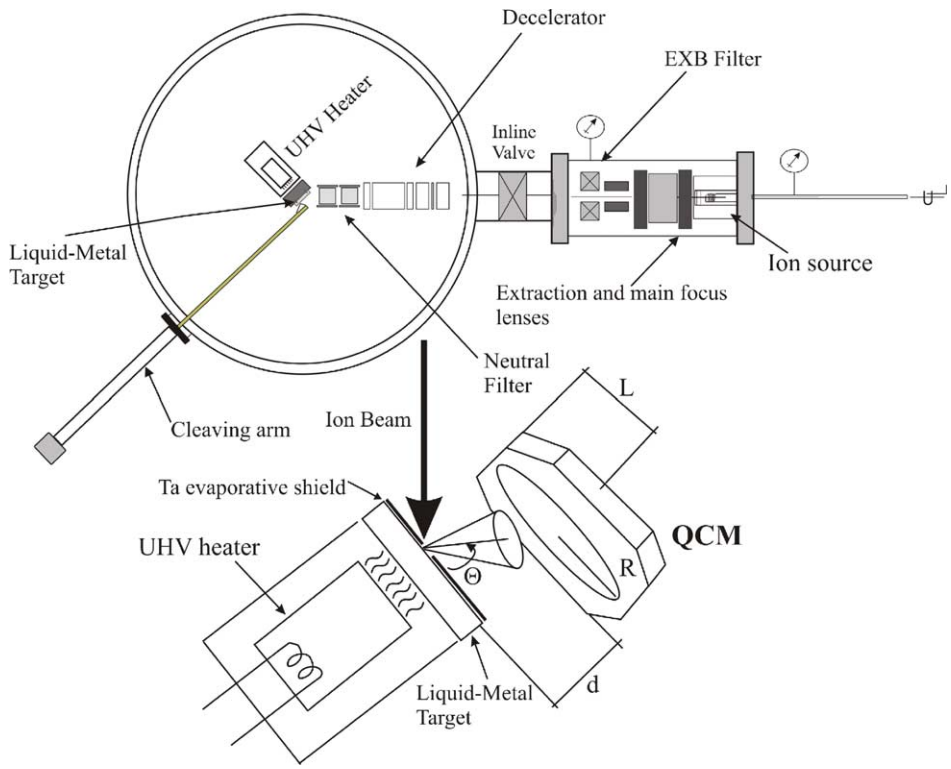

Fig. 1. The ion-surface interaction experiment (IIAX). The experimental device is shown with two differentially pumped chambers. On the right, the ion gun chamber and on the left, the main chamber where the lithium target sample is located. The inset diagram shows the position of the QCO with respect to the lithium target. The distance between the lithium target and the QCO is d, the angle of ejected flux ϕ, the radius of the crystal, R and the length from the edge of QCM to center of crystal, is designated L.

2.1. Experimental setup of IIAX

A Colutron ion source creates and accelerates gaseous or metal ions onto a 0.03-cm^2 liquid-metal target. Gaseous ions are obtained by means of electron-impact ionization while the lithium metal ions are obtained by thermionic emission from a LiCl powder. The bombarding ions are mass-selected through an $E \times B$ filter and decelerated near the target by a five-element, cylindrical, electrostatic lens system. Foil samples 0.075 cm thick with an area of 1 cm^2 are inserted in the main chamber under an argon atmosphere. The target insertion for non-reactive materials such as Sn–Li and Sn are performed at atmospheric pressure, but lithium targets require a pressurized system with continuous purging to prevent reaction with any ambient water vapor. The target can be rotated to provide variation in the angle of incidence. A 45° incidence was selected based on the average angle of incidence a sheath-accelerated, gyrating particle makes where the magnetic field lines cross the divertor plates at oblique incident angles [12–14].

A quartz crystal microbalance dual crystal unit (QCM-DCU) is rotated in front of the target, as shown on the inset of Fig. 1, to collect the sputtered flux, measuring the absolute sputtering yield. The QCM-DCU is mounted on a manipulator and thus its spatial position and orientation with respect to the target are known. A brief description of the QCM is given in the next section. A plasma cup provides plasma cleaning of the target, removing any oxides or other impurities from the surface. This method also allows for deuterium treatment (implantation) within the top surface of the liquid-metal, simulating plasma-facing wall conditions within a fusion reactor. For tin–lithium, the segregated lithium layer (∼10 to 40 Å) does not show any significant uptake of deuterium, probably due to the low solubility level of D in tin. Deuterium retention in Sn–Li, however, requires further investigation and is beyond the scope of this work. Deuterium treatment of 0.8 Sn–Li and its effect on lithium sputtering have been studied in IIAX and are treated in more detail in the literature [8]. Although experiments have been carried out on the effect of D-treatment on the erosion of the segregated lithium layer in liquid tin–lithium, much more work is needed to fully comprehend whether liquid tin–lithium could trap a significant amount of deuterium in the liquid state.

A small high-temperature UHV substrate heater heats the sample past its melting point (180, 320, and 232 °C for Li, Sn–Li, and Sn, respectively). Upon melting, a thin oxide layer forms on the exposed lithium or tin–lithium surface, which is scraped off by an in situ arm rotated in front of the target. A tantalum evaporative shield is placed on the sample to reduce the evaporative flux component during erosion of the sample. Fig. 1 shows the tantalum shield with the liquid-metal sitting on a backing plate facing the heater. The plane of the target and shield is parallel to the plane of the QCM crystal as shown. The evaporative shield hole is about 1.5 mm in diameter, slightly larger than the 0.1 cm beam spot size. A He–Ne laser is used prior to chamber evacuation to align the ion-beam path with the 0.15 cm shield hole [7]. In addition, alignment is also evident from the signal of collected material measured by the deposition quartz crystal oscillator (QCO) signifying the sputtering of lithium. The signal measured corresponds only to lithium or tin sputtering since the sputtering yield of tantalum by light particles at these energies and for the materials investigated is between 0.00025–0.0015 atoms/ion—about one to two orders of magnitude less than sputtering from liquid lithium, tin–lithium or tin.

A small type-K thermocouple is placed between the sample and the back-plate facing the heater. A type-J thermocouple is placed on the side near the evaporative shield where the exposed lithium sample is located. For temperatures between 200 and 450 °C, use of both thermocouples is appropriate. Another type-K thermocouple is positioned on the in situ mechanical arm, which removes the liquid-metal slag upon melting. This also serves as a third method to measure the liquid-metal temperature. The thermocouples at all three locations measured temperatures within 20–30% of each other. For example, one of the temperatures measured by the type-K thermocouple on the evaporative shield was 210 °C, while the temperature measured on the side near the evaporative shield was 170 °C and from the type-K on the in situ mechanical arm, 190 °C. Despite all these measurements, error still exists from the uncertainty of the temperature measurement on the surface of the liquid-metal sample since heat transfer will occur from the surface of the liquid-metal to the stainless steel arm or tantalum shield. Therefore, error bars of the order of 20–30% are included in the temperature values or are

assumed if not indicated in the figures throughout this document.

The partial pressures of gas species within the system are monitored with a quadrupole gas analyzer. Typical total base pressures before the ion beam chamber is opened to the main system range from 10^{-6} to 10^{-5} Pa. An incident ion flux of the order of 10^{14} ions/(cm^2 s) can be achieved with an average beam spot diameter of 0.1 cm, resulting in current densities of the order of 20 μA/cm^2. During the course of a one-h exposure, the total dose to the target is of the order of 10^{16} ions.

2.2. Quartz crystal microbalance dual control unit

The QCM-DCU consists of two gold-coated quartz AT-cut crystals, in thermal contact, with a fundamental frequency of the order of 6 MHz (Fig. 2). One sensor acts as the deposition crystal, the other as a reference crystal. Since the sticking coefficient is 25% for sputtered lithium atoms on the gold-covered QCO crystal, a thin carbon layer is evaporated ex situ on both the deposition and reference crystals increasing the sticking coefficient from 25% to 85%. For sputtered tin atoms, no carbon layers are used, since, sputtered tin atoms stick better to gold.

A background trace monitors the evaporative flux using both crystals for a period of 15–24 h when the QCM is situated in front of the target. One crystal collects the evaporative flux, while the other remains a reference without deposition. For evaporation measurements, the sticking coefficient of thermally emitted lithium and tin atoms is estimated to obtain the measured evaporative flux or partial pressure from the liquid-metal surface. Fig. 3 shows a schematic for evaporation results of liquid lithium as a function of temperature. Error due to the estimate of collection angle as well as sticking coefficient can lead to uncertainties of near 40–50%. For lithium, estimating the evaporation, is important since its magnitude is equal to or larger than that of the sputtered flux in IIAX; however, both molecular dynamic modeling [15] and direct experimentation [16] show that the sticking coefficient for thermal and hyperthermal-energy lithium atoms is significantly less than those with energies typical of sputtered particles, resulting in a clear distinction between

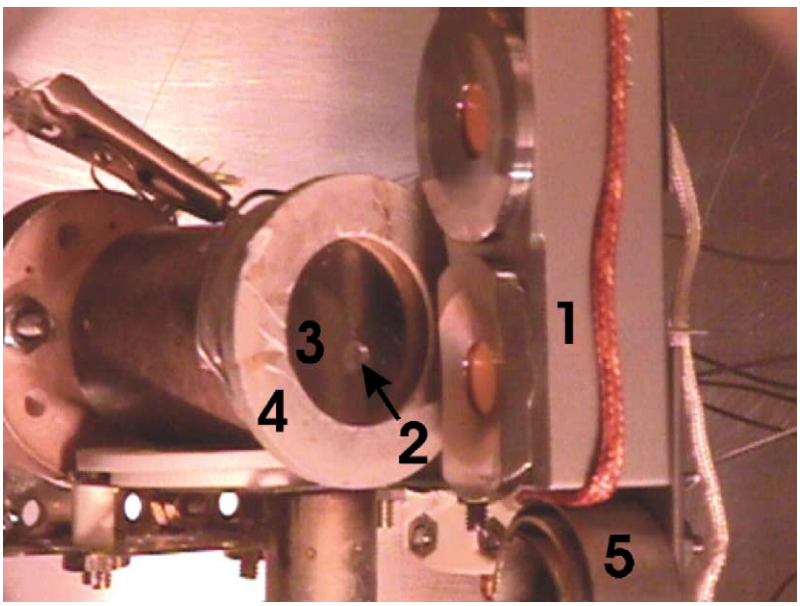

Fig. 2. The quartz crystal microbalance–dual crystal unit (QCM–DCU) diagnostic system in IIAX. (1) shows the two crystals in thermal contact; (2) shows the liquid-metal target embedded under (3) the evaporative tungsten shield; (4) is the boron nitride holder and inside of the holder is the UHV heater; (5) shows the hollow cathode plasma cup for sample exposure to a low-temperature plasma.

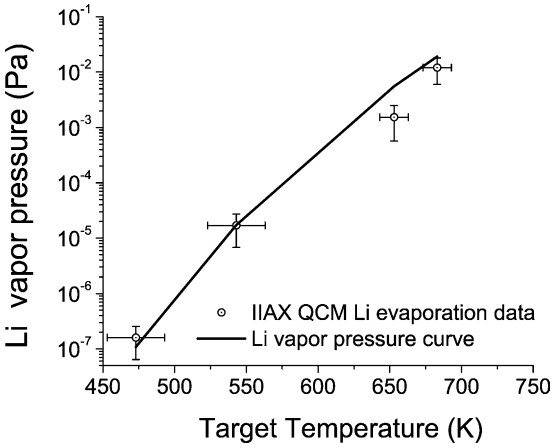

Fig. 3. Lithium vapor pressure data with calculated curves at temperatures between 200 and 400 °C. The data accounts for sticking of evaporated thermal atoms onto the quartz gold-covered crystal estimated with molecular dynamics calculations.

evaporative and sputter fluxes. For tin experiments, this difficulty is non-existent since the evaporation flux for temperatures investigated is about six orders of magnitude less than the sputtered tin flux.

Deposition of the sputtered and evaporative fluxes are measured by a decrease in frequency as mass is collected on the crystal while the beam is on and aligned onto the liquid-metal sample. After the target receives the proper dose, the beam is turned off, and both crystals are kept running until the change in frequency due to the evaporative flux alone is obtained again. Sample traces of the frequency difference, Δf, of the dual QCO unit against time plotted with ion current on the sample are included in Allain's Ph.D. thesis [8]. The frequency variation of the deposition crystal correlates with the mass loss of the sample as shown quantitatively in the next section. X-ray photoelectron spectroscopy (XPS) measurements show that the material deposited on the QCO is lithium oxide due to the high reactivity of lithium with oxygen on the crystal. Moreover, for tin sputtering, Auger measurements show that SnO is the material deposited on the QCM crystal [17].

2.3. Analysis of liquid-metal sputtering measurements

Analysis of the absolute lithium-sputtering yield from both liquid lithium and liquid tin–lithium and the absolute tin-sputtering yield from liquid tin samples is done by correlating the frequency variation in the crystal signal with the time period of ion beam dose. The calculation of the absolute sputtering yield is then possible after accounting for sputtering of QCM deposited material by incident highly energetic reflected particles, sticking coefficient of sputtered atoms onto the QCM crystal and the secondary ion fraction of sputtered atoms (for lithium-based surfaces). A mass balance is used to set up the analytical expression for the absolute sputtering yield. The mass deposited on the crystal, which corresponds to the mass loss from the lithium sample, M_{d} due to both evaporation and physical sputtering is shown to be

$$M_{\mathrm{d}} = \frac{DS^{\mathrm{QCM}} Y \Omega m_{\mathrm{LMO}} f_i}{N_{\mathrm{A}}} \tag{1}$$

where D is the total ion dose. The sticking coefficient, S^{QCM}, is estimated using VFTRIM-3D, and is defined as $1 - R_j^{\mathrm{QCM}}$, where R_j^{QCM} corresponds to the reflection coefficient for sputtered species j off the QCM crystal surface. Y is the total (ions + neutrals) sputtering yield in sputtered particles per ion. Ω is the fraction of the normalized distribution of sputtered particles subtended by the QCM crystal, and f_i is a factor ranging from 1.5 to 1.8 that accounts for the ion fraction of sputtered species. The mass of liquid-metal-oxide deposited on the QCM deposition crystal is m_{LMO} (in g/mol), and N_{A} is Avogadro's number. The mass deposited on the QCM crystal as measured by the Leybold Inficon XTC/2 monitor is defined as

$$M_{\mathrm{QCM}} = \frac{\Delta f}{f} M_{\mathrm{crystal}} \tag{2}$$

where Δf is the frequency change measured from the raw frequency difference between the deposition and reference crystal data. M_{crystal} is the mass of the crystal given by the manufacturer, and f is the initial frequency of the QCM crystal. The M_{QCM} term incorporates the mass loss due to sputtering from reflected incident particle neutrals from the liquid-metal surface. The reflection coefficient of incident ions, R_j (j is the species type), the sputtering coefficient of energetic neutrals impinging on the QCM crystal surface, Y_j^{QCM}, and the fraction of the normalized distribution of reflected particles subtended by the QCM, Ω_j, are factored into the

mass variation of the QCM in this manner:

$$M_{\mathrm{QCM}} = \frac{\Delta f}{f} M_{\mathrm{crystal}}(1 + R_j Y_j^{\mathrm{QCM}} \Omega_j). \quad (3)$$

A mass balance between the mass loss from the liquid-metal sample and the mass gained on the QCM deposition crystal results in the expression for the absolute sputtering yield:

$$Y = \frac{1}{D f_i S^{\mathrm{QCM}} \Omega m_{\mathrm{Li_2O}}} \frac{\Delta f}{f} M_{\mathrm{crystal}}(1 + R_j Y_j^{\mathrm{QCM}} \Omega_j). \quad (4)$$

For the self-sputtering (lithium) case, this expression becomes

$$Y_{\text{self-sputtering}} = \frac{1}{D f_i S^{\mathrm{QCM}} \Omega m_{\mathrm{LMO}}} \frac{\Delta f}{f} M_{\mathrm{crystal}}. \quad (5)$$

This expression differs from Eq. (4) because reflected incident lithium atoms are considered part of the self-sputtered signal for the purpose of quantifying lithium flux from the surface.

Eq. (5) does not include the partial sputtering yield of tin, for the case of 0.8 Sn–Li sputtering, for two reasons. First, the sputtering threshold for pure tin is high, near 200–300 eV due to its relatively high elemental surface binding energy. At 45° incidence, the sputtering yield of Sn is as high as 0.10–0.15 Sn atoms/ion at energies of 500–1000 eV, according to simulations using TRIM-SP for D and He bombardment. Second, if the beam-facing surface is a mixture of Sn and Li atoms, the amount of Sn sputtering calculated above would lead to sufficient Sn measured on the on the QCM deposition crystal for detection by XPS. The XPS measurements show that 99.6% of the mass deposited on the QCM crystal is oxidized lithium. This confirms measurements by Bastasz of tin–lithium in liquid phase, where lithium atoms segregate to the surface [18]. Thus, the surface sputtered is mostly lithium particles.

In addition, measurements in IIAX of the fraction of sputtered atoms which emerge as ions from solid 0.8 Sn–Li and liquid 0.8 Sn–Li compared to pure liquid lithium indicate that the beam-facing surface during bombardment is pure Li [9,10] once the sample is in the liquid state. The sputtered atom ion fraction of liquid 0.8 Sn–Li is 65%, and is on average equal to pure liquid lithium. In the solid-phase 0.8 Sn–Li values of 10% are obtained. These high secondary ion sputtered fraction results are consistent with predictions made for Li–Al and Li–Cu systems by Krauss and Gruen [19]. For the case of tin sputtering the secondary ion sputtering fraction is rather low; only values up to 10% have been measured under a variety of incident particle (D^+, He^+) energies and liquid tin temperatures [17].

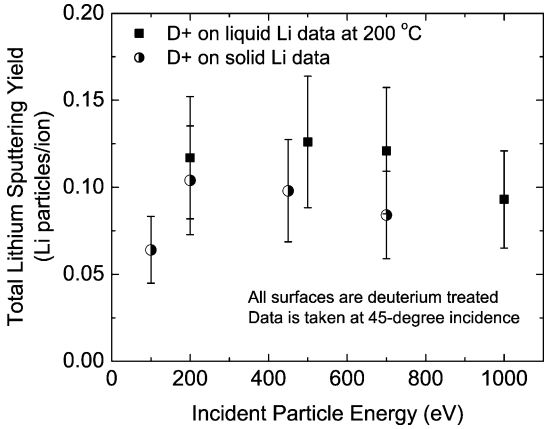

Fig. 4. D^+ bombardment of D-saturated liquid and solid lithium at 45° incidence compared to VFTRIM-3D simulation data. Total lithium sputtering yield includes both ions and neutrals.

2.4. Measurements of liquid lithium sputtering just above the melting point

Fig. 4 shows the total lithium sputtering yield measured at energies between 200 and 1000 eV for D^+ bombardment of D-treated liquid and D-treated solid lithium at 45° incidence [7,9]. The maximum lithium sputtered is found near the 400–500-eV range for liquid lithium and 200 eV for solid lithium. Fig. 5 shows experimental data for self-sputtering at energies between 200 and 1000 eV for both liquid and solid lithium. The self-sputtering yield reaches a maximum near 700 eV for both liquid and solid lithium. Fig. 6 shows the D-treated liquid and solid lithium sputtering yield for He^+ bombardment of D-treated liquid and solid lithium for energies between 200 and 1000 eV. A maximum yield from helium bombardment is noted near 500 eV for both liquid and solid lithium. The fraction of Li atoms sputtered in the ionic state from liquid-phase lithium is 0.65 ± 0.1 compared to 0.55 ± 0.1 for solid-phase lithium for 700-eV He^+ bombardment [7].

All sputtering yields for liquid lithium are slightly larger than lithium sputtering yields in the solid state.

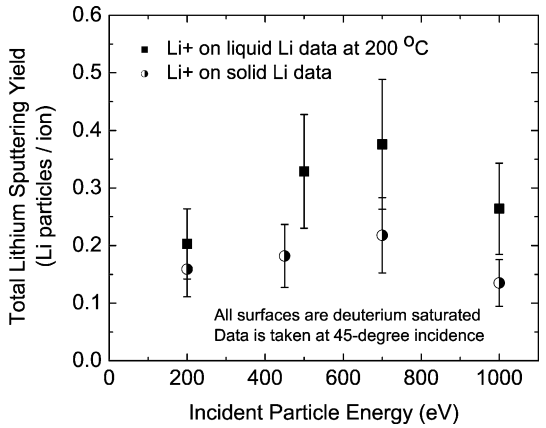

Fig. 5. Lithium self-sputtering for liquid and solid lithium at 45° incidence with surfaces treated with deuterium. Total lithium sputtering yield includes both ions and neutrals.

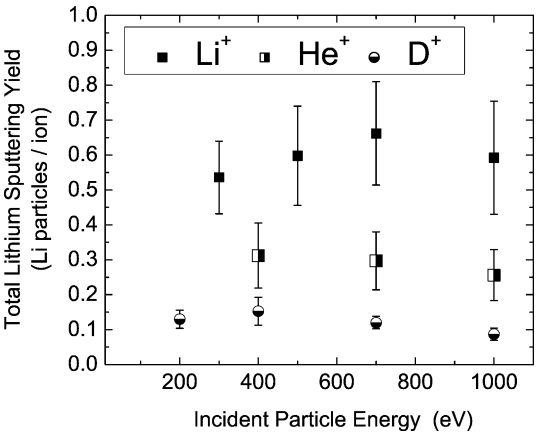

Fig. 7. Experimental data of Li^+, D^+ and He^+ bombardment of liquid-phase tin–lithium sputtering at 45° incidence. Total lithium sputtering yield includes both ions and neutrals.

In both cases, the low lithium-sputtering yield is directly related to the treatment of the surface by deuterium atoms. In the case of the solid phase, preferential sputtering mechanisms dominate the physical sputtering yield. In the case of lithium in the liquid phase, the relative bonding between atoms dominates the absolute sputtering of Li atoms [7,9,10].

Deuterium bombardment exhibits different maxima for experimental data points, depending on the surface state of the lithium sample. This suggests an enrichment of deuterium atoms in the bulk of liquid lithium that shifts the maximum of the nuclear stopping cross-section to higher energies. The effect of deuterium treatment varies from the solid to the liquid phase. Experimental data show that for solid lithium the sputtering yield of Li atoms is significantly decreased by deuterium treatment of the surface [7,20]. In contrast, although the solubility of deuterium in liquid-phase lithium is high, D atoms readily migrate to the bulk due to the high diffusivity and strong concentration gradient. Thus, as the temperature is raised beyond the melting point, the effect of deuterium treatment on reducing lithium sputtering diminishes. Although the effect of deuterium treatment in solid lithium near the melting point is important, at temperatures beyond 250–300 °C, this effect is negligible—ion-bombardment-induced mechanisms take effect and lead to enhanced erosion of liquid lithium as demonstrated by atomistic simulations [21]. This phenomenon has also been measured in IIAX for 0.8 Sn–Li and Sn in the liquid state [16] and will only be briefly discussed in this review.

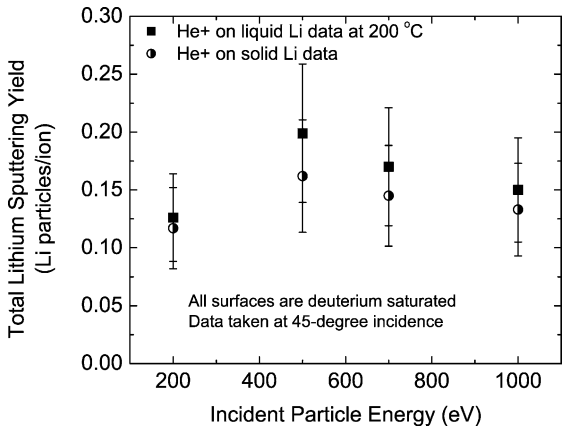

Fig. 6. He^+ sputtering of solid and liquid lithium near the melting-point (180 °C) at 45° incidence. Total lithium sputtering yield includes both ions and neutrals.

2.5. Measurements of liquid tin–lithium sputtering just above the melting point

Fig. 7 shows experimental data for the absolute sputtering yield of Li at energies between 200 and 1000 eV for D^+, He^+ and Li^+ bombardment of liquid tin–lithium at 45° incidence. The maximum Li sputtered for deuterium bombardment is found near 400 eV, similar to pure liquid lithium results discussed earlier [9]. Experimental data for helium bombardment results

show a maximum of the yield near 400 eV. This sputtering yield maximum is also close to that obtained for helium bombardment of solid and liquid lithium. The Li sputtering yield reaches a maximum near 700 eV, similar to results of pure solid and liquid lithium sputtering [7,9]. The measured fraction of sputtered particles emerging as ions for D^+, He^+ and Li^+ bombardment is less than 10% for solid 0.8 Sn–Li, but increases to around 65% for liquid 0.8 Sn–Li as discussed earlier.

The largest contribution to the absolute sputtering of lithium comes from bombardment by lithium ions onto liquid 0.8 Sn–Li. The maximum absolute sputtering yield of Li by lithium bombardment is about a factor of two greater than for helium bombardment and a factor of four greater than for deuterium bombardment. This is due to a greater transfer of energy between Li^+ bombarding ions and Li atoms on the surface, compared to D^+ and He^+ bombarding ions. In addition, subsurface layers containing 80 % Sn act as a reflective wall, thus, incident bombarding particles backscatter with high outward momentum, leading to more lithium sputtering. For example, incident Li and He atoms transfer about 16% and 10% of their energies, respectively, to sub-surface Sn atoms leaving any backscattered Li and He atoms with sufficient energy to cause significant sputtering of surface Li atoms.

All lithium sputtering yields from liquid tin–lithium samples are larger than those on D-treated liquid lithium in the liquid phase just above their respective melting points. This is due to energetic backscattered atoms as explained earlier. In addition, since the solubility of deuterium in liquid tin–lithium is relatively low [22], its contribution to decreasing the absolute sputtering yield of Li is also very low.

As in the sputtering of pure liquid lithium, the ion fraction of sputtered atoms is important. Particles that sputter as ions will quickly return to the surface in a fusion device due to the plasma sheath and near-parallel magnetic field. For the case of liquid tin–lithium, the ion fraction was measured to be 65% compared to <10% for solid tin–lithium. This relatively large ion fraction coincides with that measured in pure liquid lithium [7,9]. This provides further evidence that Li atoms segregate to the surface of liquid tin–lithium, forming a thin layer of lithium atoms; therefore, the surface of liquid tin–lithium will behave in a similar way to the surface of pure liquid lithium with respect to the ion-induced secondary sputtered ion fraction.

2.6. Ion-bombardment-induced temperature enhancement of liquid lithium and liquid tin–lithium sputtering

Measurements of liquid lithium and liquid tin–lithium just above the melting point did not show a large difference in the absolute lithium sputtering yield compared to the solid phase. This was the case over a variety of incident species (H^+, D^+, He^+ and Li^+) and incident particle energies (100–1000 eV) [16]. As the temperature of the liquid-metal was increased further, an unexpected rise in the absolute lithium sputtering yield of the bombarded liquid-metal was measured in IIAX. This result also confirms earlier liquid lithium temperature-dependent data from PISCES-B [4], although the ion-beam experiments in IIAX were carried out with ion fluxes that were four orders of magnitude lower than those found in PISCES-B. Similar, results were obtained for Sn and Ga in the liquid state. Results for tin will be discussed shortly.

One particular set of data is the deuterium-ion bombardment of D-treated liquid lithium. The results for 300–1000 eV D^+ bombardment of D-treated liquid lithium at temperatures between 200 and 420 °C at 45° incidence are shown in Fig. 8. The data show an enhanced lithium-sputtering yield that begins near 300 °C. As discussed earlier, the lithium sputtering

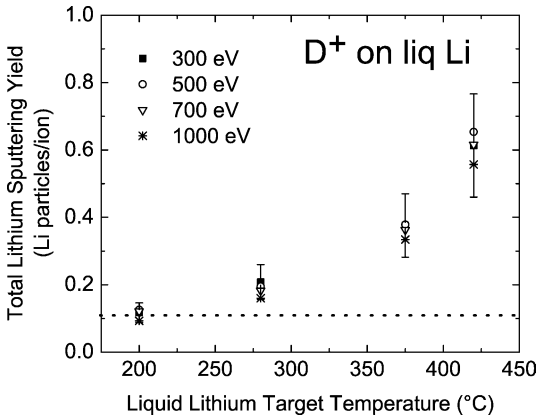

Fig. 8. Liquid lithium sputtering from D^+ bombardment at 45° incidence plotted vs. target temperature for a variety of incident particle energies. Dotted line shows the maximum total (ions + neutrals) lithium sputtering yield of 0.138 ± 0.056 at room temperature with incident particle energy. Total lithium sputtering yield includes both ions and neutrals.

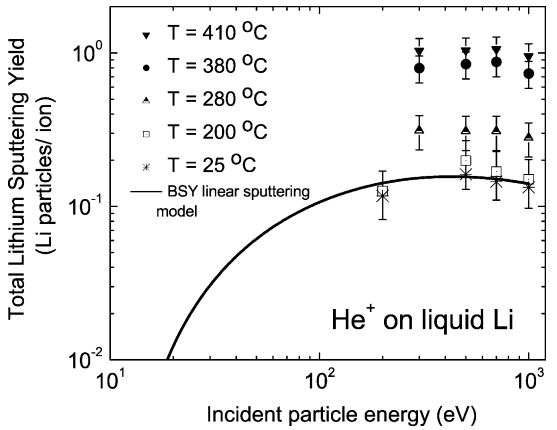

Fig. 9. He^+ on liquid lithium results for 300–1000 eV bombardment at 45° incidence for temperatures 200–420 °C plotted with the Bohdansky–Sigmund–Yamamura model of linear cascade theory. Total lithium sputtering yield includes both ions and neutrals.

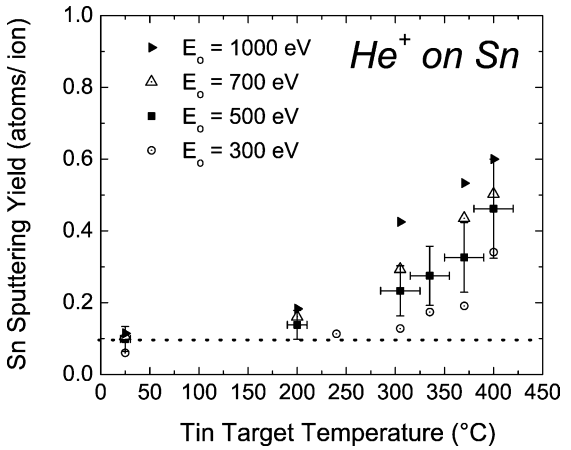

Fig. 10. Experimental results for the sputtering yield of liquid tin compared to solid tin due to helium ion bombardment; data are parameterized by the ion energy and presented as a function of target temperature. Representative error bars are shown for the 500 eV case—errors at the other energies are of similar magnitudes. Dotted line shows the total (ions + neutrals) tin sputtering yield of 0.106 ± 0.048 at room temperature with He^+ energy of 700 eV.

yield component is obtained by subtraction of the evaporation signal from the total lithium erosion signal (sputtering + evaporation); therefore, only ion-bombardment-induced effects are responsible for the measured lithium erosion enhancement.

Fig. 9 shows results for 300–1000 eV He^+ bombardment at 45° incidence for temperatures between 200 and 420 °C. This data is plotted with the Bohdansky–Sigmund–Yamamura model for linear cascade theory [7]. The data clearly show the nonlinear nature of liquid lithium erosion as the temperature is increased, similar to bombardment with D^+. In addition, the sputtering yield maximum tends to shift toward lower energies, indicating that ion-bombardment-induced surface mechanisms are responsible for the enhancement. To determine if the enhancement occurs for other liquid-metals, tin was chosen due to its low melting point and, more importantly, due to its low vapor pressure, which, at 200 °C, is about six-orders of magnitude less than for lithium [17]. Thus, any contribution due to thermal evaporation is not measurable with the instruments used.

2.7. Measurements of liquid tin sputtering

Another candidate PFC liquid-metal is tin, which melts at 232 °C. Fig. 10 shows results for Sn sputtering from helium bombardment at various incident particle energies and sample temperatures. The data show a clear temperature dependence of the sputtering yield of liquid tin due to helium ion bombardment, similar to experiments with liquid lithium and liquid tin–lithium discussed earlier. Similar results were found for deuterium bombardment [17]; however, the magnitude of the tin sputtering yield from the liquid state compared to the solid state of tin is lower if the solid tin surface is an oxide. This is because tin is one of only a few metals whose oxides have a higher sputtering yield than the pure metal [23]. Moreover, when an oxidized tin sample is melted, oxygen is effectively desorbed from the tin sample. After the surface resolidifies, the tin is nearly free of oxygen in the solid state, and its sputtering yield is *less* than an oxidized surface of solid-state tin. Once in the liquid state and after increasing the temperature, enhanced erosion of liquid tin is measured for both deuterium and helium bombardment [24].

The temperature-dependence of the sputtering yield of liquid tin due to low-energy, light-ion bombardment behaves similarly to that of liquid lithium and liquid tin–lithium. Similar measurements of enhanced erosion for low vapor pressure metal were found for gallium in PISCES-B [3]. Although the temperature dependence is not as strong as that found in liquid lithium in IIAX [16] or with a deuterium plasma in PISCES-B [25,26], where the sputtering yield increased by about

an order of magnitude over a similar temperature range, the temperature enhancement of liquid tin's sputtering yield is significant and measurable. Thus, liquid-metal sputtering measurements from a number of experimental facilities indicate that enhanced erosion levels are expected as the temperature of the irradiated sample is increased.

2.8. Temperature-dependent sputtering mechanisms

The physical explanation of the temperature enhancement of sputtering yields of liquid-metals is not yet complete; however, a model by Allain and Ruzic has been developed [21] and helps explain temperature enhancement measurements of liquid lithium. The Allain–Ruzic model suggests that the main factors that change as a result of increasing the target temperature are the bonding nature of atoms with their nearest neighbor and the change in the spatial distribution of deposited energy. Multi-body attractive forces at the surface are weakened with increasing temperature due to the mobility of near-surface atoms. Ordinary sputtering is initiated by linear collision cascades, in which all the atoms hit atoms at rest. However, we find that in liquid lithium the physical model of a cascade in which all the atoms strike other atoms in motion is consistent with the enhanced sputtering lithium yields we measure at low incident particle energies, across a very narrow temperature range (e.g., 200–400 °C). Furthermore, incident particles deposit an increasing fraction of their energy in the near surface region at low energies and in multi-body collisions. Further detail and investigation is necessary to verify the Allain–Ruzic model. For example, the sputter depth is only a few monolayers from the liquid surface. The spatial resolution of the liquid–vapor interface for liquid-metals has been characterized by a stratified layer due to the electronic properties at the surface of a conducting liquid. How this stratified layer affects reflection and sputtering of low-energy, incident charged particles and how it is connected with the temperature-dependent erosion results discussed here are beyond the scope of the paper and require further study. In addition, continued work with atomistic simulations will assess whether these mechanisms can explain enhanced erosion measured in other liquid-metals, such as tin, gallium and tin–lithium.

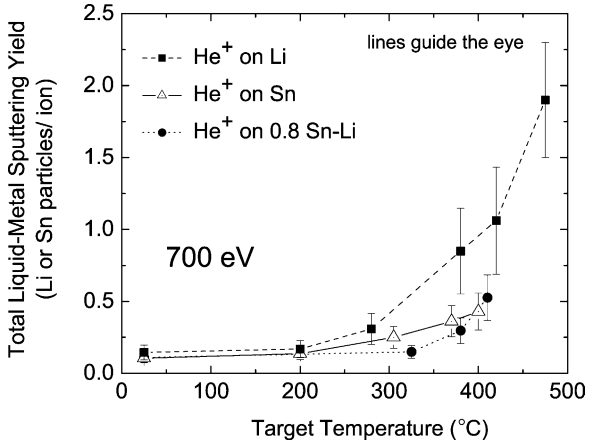

Fig. 11. Comparison of the total sputtering yields of solid and liquid-state Li, Sn and 0.8 Sn–Li bombarded by 700 eV, 45° incident He^+ plotted vs. target temperature. For reference the melting points of Li, Sn and 0.8 Sn–Li are: 180, 232, and 330 °C, respectively. Total liquid-metal sputtering yield includes both ions and neutrals.

2.9. Comparisons of sputtering among candidate liquid-metal PFC materials

A comparison between the liquid-metals studied further elucidates the behavior of the physical sputtering yield of liquid-metals and ion-bombardment-induced mechanisms. In this case, Li, Sn and 0.8 Sn–Li in the solid and liquid states are compared. Fig. 11 shows the sputtering yield of lithium from Li and 0.8 Sn–Li and the tin sputtering yield from Sn bombarded by He^+ at 700 eV and 45° incidence. One common aspect among all the liquid-metals studied is that the total sputtering yield does not vary much between the solid and liquid states at temperatures close to the metal's melting point. In the case of lithium, the lithium sputtering yield is 0.145 ± 0.051 in the solid state (25 °C) and is 0.169 ± 0.059 in the liquid state at 200 °C is, which is 20 °C higher than lithium's melting point. As discussed earlier, any oxide on the tin sample will lead to a larger tin yield than in its pristine state. Thus, for a pristine tin sample, the sputtering yield is 0.106 ± 0.032 in the solid state at 25 °C and is 0.251 ± 0.075 in the liquid-state at 305 °C for data taken in IIAX. The melting point for tin is 220 °C. In the case of the tin–lithium alloy (0.8 Sn–Li); the lithium sputtering yield is 0.110 ± 0.033 at 25 °C, and for liquid 0.8 Sn–Li at 335 °C, the lithium sputtering yield is 0.150 ± 0.045 with the melting point of the alloy being close to

330 °C. Data taken in the PISCES-B device with liquid gallium also showed similar behavior under deuterium ion bombardment. The invariant behavior of the sputtering yield across the liquid-metal melting point is also noted for bombardment with other species, namely: D^+ and Li^+.

As the temperature is increased beyond the melting point of the metal, the enhancement of liquid-metal erosion is noted; however, its increase with temperature seems to vary from metal to metal. For example, lithium sputtering from liquid lithium increases more slowly with temperature than the lithium sputtering yield from liquid 0.8 Sn–Li. Liquid tin has a slower sputtering yield enhancement with temperature than either tin–lithium or lithium; however, further data is needed for 0.8 Sn–Li and Sn samples at higher temperatures to determine this conclusively. How lithium in the alloy behaves differently, with respect to erosion, than a pure liquid lithium surface is under current investigation. In addition, further work by Allain currently investigates threshold sputtering regimes for liquid lithium sputtering, ion flux dependence of liquid lithium sputtering and its functional dependence with temperature.

3. Particle retention measurements of flowing liquid lithium in FLIRE

In addition to erosion characteristics, another critical property of any liquid-metal used in a fusion machine environment is its retention of helium and hydrogen particles. The flowing liquid retention experiment (FLIRE) was designed and built to measure these and other properties of a free-surface-flowing liquid. Measurements in FLIRE presented in this paper focus on the helium retention properties of flowing liquid lithium.

3.1. Experimental description of FLIRE

FLIRE consists primarily of two vacuum chambers, the upper chamber and the lower chamber, interconnected by a small aperture and independently pumped. Fig. 12 shows a diagram of the FLIRE experiments showing the location of the upper and lower chambers. To drive the flow, a third chamber, called lower reservoir, is filled with molten lithium and pressurized with argon gas. Lithium transfer lines connect the lower reservoir to the upper chamber through a pneumatic valve. When the pneumatic valve is opened the

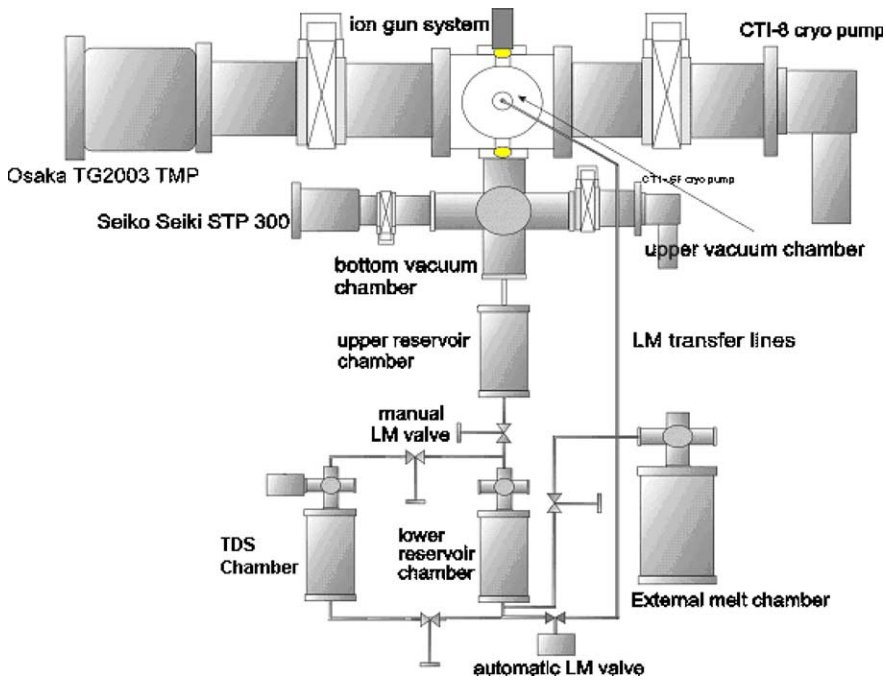

Fig. 12. Updated block diagram of the FLIRE main components showing the newly installed TDS chamber.

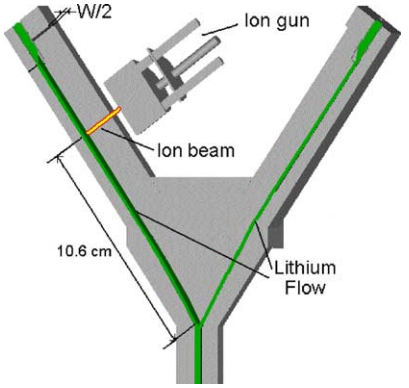

Fig. 13. Cross section of the ramp assembly inside the FLIRE upper chamber. The rectangular hole at the bottom is 3 × 10 mm, so W = 10 mm. The distance from beam strike point to the point of exit is 10.6 cm.

pressure in the lower reservoir drives the lithium through the transfer lines and into the upper chamber. The average flow rate of the lithium is controlled by the initial driving pressure; typical driving pressures are ∼150 Torr, resulting in flow speeds ∼ 50 cm/s. Because the upper chamber is ∼150 cm higher than the lower reservoir, a minimum pressure of ∼70 Torr is required to raise the lithium up to the level of the upper chamber.

In the upper chamber, the liquid lithium can flow in one or two separate streams along two rectangular open channels, as shown in Fig. 13. The streams reach the exit orifice and flow into the lower chamber (not to be confused with the lower reservoir) through an exit channel. When the stream flows through the exit orifice, the liquid-metal forms a vacuum seal between the upper chamber and the lower chamber. After the flow stops, the seal remains due to the small amount of lithium held in the exit channel by surface tension. The vacuum seal was confirmed by observing the pressure in each chamber before (starting with a clear exit channel) and after lithium flow with gas fed into the upper chamber. Fig. 14 shows the Argon pressures in the upper chamber and lower chamber before and during lithium flow, starting with an initially clear exit channel. Initially, the pressures in the two chambers are high (5×10^{-5} Torr in the upper chamber and 3×10^{-6} Torr in the lower chamber) because there is no seal in the exit channel. The upper-chamber pressure is higher than the lower chamber pressure in the no-seal condition because Ar gas is fed into the upper chamber and must pass through

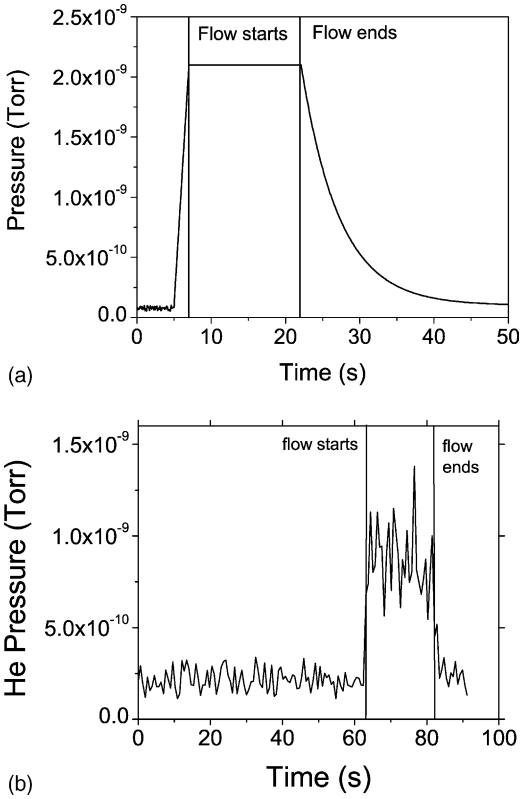

Fig. 14. (a) Idealized pressure evolution curve in the FLIRE lower chamber, assuming constant pumping speed and constant release rate from the metal. (b) Actual helium trace in the lower chamber during a FLIRE run. The average flow velocity was 25 m/s, and the energy of the ions was 1500 eV. Flow start and end points are marked in the figure by vertical lines.

the small exit channel to reach the lower chamber. Once the lithium flow reaches the exit channel, the pressure in the lower chamber decreases and the pressure in the upper chamber increases because the gas flow is only in the upper chamber, but both chambers are pumped independently. This test confirms that a liquid lithium seal forms between the two chambers. Even after the flow stops, the seal remains because of the high surface tension of liquid lithium. This liquid-seal separation of the two chambers allows the measurement of the release rate of the implanted gas in the lower chamber without interference from the background gas that is necessary to operate the ion gun in the upper chamber (∼2×10^{-5} Torr).

As shown in Fig. 13, one of the streams is exposed to an ion gun located approximately 10 cm from the exit

channel. The ion gun injects helium into the lithium flow with energies between 500 and 4 keV and is capable of currents between 1 and 10 μA. The implanted helium diffuses in and out of the flow stream as the lithium travels down the channel until the flow reaches the exit orifice. During this time, most of the helium diffuses out of the lithium stream and is released into the upper chamber. When the flow reaches the exit orifice, it pours into the second (lower) chamber, where a magnetic sector residual gas analyzer (MS-RGA) monitors the helium partial pressure as the remaining implanted helium is release into the lower chamber. This RGA was calibrated to an all-metal Bayard–Alpert micoion gauge, and the pressure signals are corrected by a known factor (five for the case of helium) to account for gauge calibration.

A turbo pump attached to the lower chamber maintains a base vacuum of $\sim 10^{-9}$ to 10^{-8} Torr when retention measurements are not in progress; however, to increase the sensitivity of the helium partial pressure (retention) measurement, the pumping rate in the lower chamber is reduced by partially closing a gate valve between the lower chamber and its turbo pump. If the pumping speed was not reduced, the helium would be pumped out before the MS-RGA could accumulate a significant signal. A decreased pumping speed in the lower chamber results in a higher base pressure of $\sim 10^{-6}$ Torr during the measurement. Because the only source of helium in the lower chamber is desorption from the lithium, the helium partial pressure measurement from the MS-RGA is insensitive to the total background gas pressure in the chamber. Before each measurement, the background helium signal is measured over a period of one minute so that it can be subtracted from the measurement when the data are analyzed.

Several subsystems work together in FLIRE to obtain an adequate measure of the release rate in the lower chamber, which yields information about particle retention. A very detailed description of these subsystems, such as the thermal desorption spectroscopy (TDS) system, can be found elsewhere [27]. The TDS chamber shares the MS-RGA capability with the lower chamber, and can ramp up the temperature at a fixed rate to correlate desorption rate with temperature. The use of the TDS chamber to study hydrogen retention and long-term helium and hydrogen trapping is currently underway.

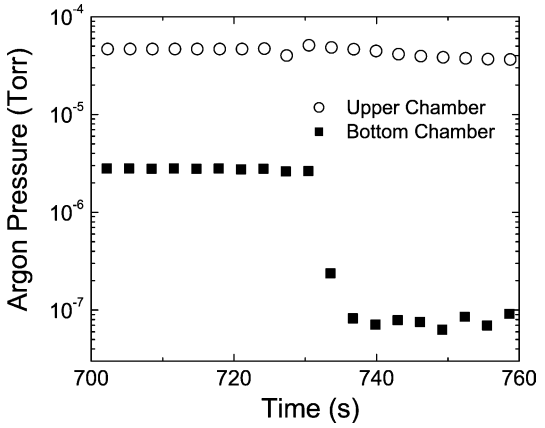

Fig. 15. Demonstration of seal formation between the FLIRE upper and lower chamber. Liquid Li flow started at $t = 730$ s. Once the flow starts, the Ar signal in the lower chamber drops drastically.

3.2. Retention of Helium in flowing liquid lithium

FLIRE directly measures the desorption rate of implanted helium in the lower chamber. If the release rate from the metal is constant, and the pumping speed in the lower chamber is kept constant, then the partial pressure of the implanted species reaches a steady-state level. Given the steady-state pressure P in Torr and the pumping speed S in cm^3/s, and assuming that the gas particles reach thermal equilibrium with the chamber walls at room temperature (20 °C), the release rate in the lower chamber q can be calculated in particles per second as:

$$q = (3.3 \times 10^{16}\,\text{atoms/Torr cm}^3)PS \quad (6)$$

Fig. 15(a) shows an idealized pressure evolution graph representing a constant release rate from the metal. In Fig. 15(b), an actual trace obtained in FLIRE by bombarding a Li flow with a He beam is shown. Although there is some scatter in the pressure trace, the shape of the curve, a flat plateau that then decays, matches the idealized pressure evolution.

Throttling the pump valve to decrease the pumping speed in the lower chamber is necessary for achieving a measurable signal of the very small quantity of the implanted species released from the flow. A quantitative measurement of the retention requires a known pump rate. The pressure decay rate provides an effective means of measuring the pumping speed in the FLIRE lower chamber. Fig. 16 shows the pressure

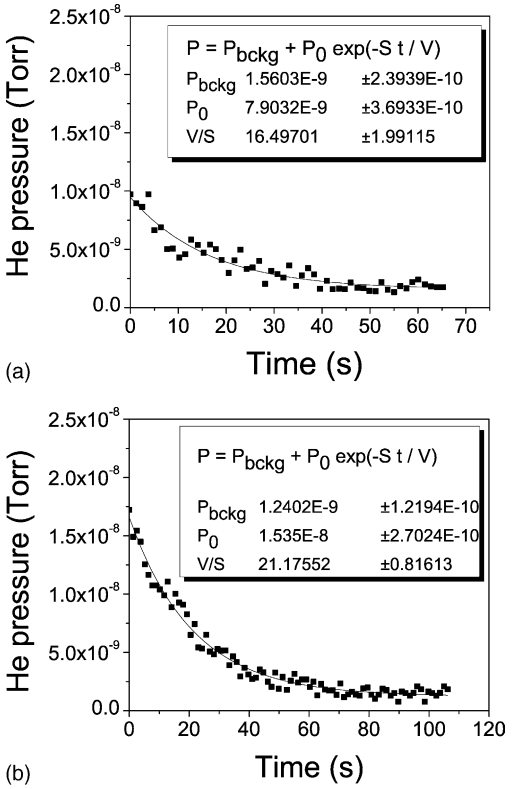

Fig. 16. (a) Pumping curves for Set A. Time constant for the pressure exponential decay (V/S) is 17 ± 2 and 21 ± 1 s resulting in pumping speeds of 0.42 ± 0.06 l/s for Set A. (b) Pumping curves for Set B. Time constant for the pressure exponential decay (V/S) is 17 ± 2 and 21 ± 1 s, resulting in pumping speeds of 0.33 ± 0.02 l/s for Set B. Small mismatch in valve aperture may account for the difference.

decay in the measurement chamber from a controlled leak with two slightly different pump-valve openings. By fitting these data with an exponential decay curve (Eq. (7)), the pumping speed, S, for a given valve opening can be calculated from the decay constant, S/V, where V is the available volume in the chamber, P_{bckg} is the base pressure in the chamber with no leak and P_0 is the initial pressure from the controlled leak.

$$P(t) = P_{\text{bckg}} + P_0\, e^{-St/V} \tag{7}$$

The pumping speed is measured after each run because the pump valve cannot be positioned precisely enough to achieve the same pumping speed between each batch of runs. The pump valve is opened fully between data sets to minimize buildup of impurities in the lithium due to higher base pressures with a throttled pump valve.

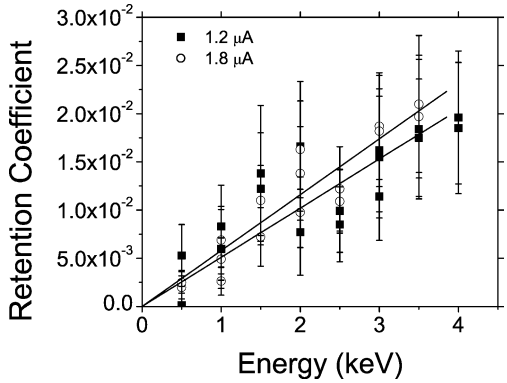

Fig. 17. Retention coefficient as a function of energy for different injection currents (1.2 μA for Set A and 1.8 μA for Set B).

For the cases in Fig. 16, the pumping speeds were 0.42 ± 0.06 l/s for data set A and 0.33 ± 0.02 l/s for data set B. These pumping speeds are used to calculate the retention coefficient, as discussed below.

The helium experimental campaign in FLIRE involved exposure of liquid lithium to a helium ion beam at different beam energies and beam currents. Lithium temperature was held at $230 \pm 10\,^{\circ}$C for these measurements. For each run, a retention coefficient R was calculated as the ratio of the release rate in the lower chamber q to the injection rate by irradiation in the upper chamber j:

$$R = \frac{q}{j}. \tag{8}$$

Values of R for different injection currents (1.2 μA for Set A and 1.8 μA for Set B) are presented in Fig. 17. Pumping speed values for the calculation of retention were obtained from the pumping curves in Fig. 16. The retention coefficient shows a linear dependence with implantation energy, as expected. Values of the retention coefficient vary from 0.25% for 500-eV particles to 2% for 4-keV particles with a flow velocity of 44 ± 6 cm/s (flow on only one channel) and a flow length of approximately 10 cm.

The dependence of retention on flow velocity is also of interest in designing advanced liquid divertors. As will be discussed in the data analysis section, helium retention should scale with the square root of the flow velocity for the condition present in FLIRE. To verify this scaling in the FLIRE experiment, retention as a function of energy was measured with lithium flow on

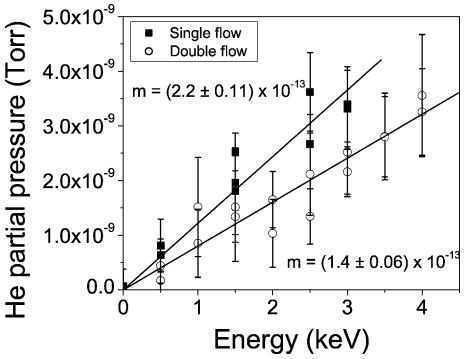

Fig. 18. Steady-state pressure in measurement chamber as a function of ion energy for experiments with single and double flow. Single flow speed is twice that in the double flow case, and slopes, *m*, differ by a factor of approximately $\sqrt{2}$.

both ramps and lithium flow on only one ramp. The flow rate in the single-ramp case was twice that of the flow-rate in the two-ramp case, and the ion-beam current was the same in both cases. By decreasing to only one flow channel with twice the flow rate, the total mass flow rate of the lithium was held constant between the two measurements, while other experimental variables that could interfere with the measurement, such as increased pooling near the flow exit, were held constant.

Fig. 18 shows the helium pressure in the measurement chamber during the single and double flow runs. Because the injected ion current was the same in both cases, the steady-state pressure is directly proportional to retention. Applying a linear fit to these data yields a slope of $(2.2 \pm 0.1) \times 10^{13}$ atoms/(s eV) for the single flow case and $(1.4 \pm 0.1) \times 10^{13}$ atoms/(s eV) for the double flow case. The ratio of slopes is then 1.6 ± 0.1, which is close to the expected value of the square root of the velocity ratio, 1.414.

3.3. Data analysis of particle retention in FLIRE

Extrapolation of FLIRE retention data to other systems requires a model to determine the appropriate scaling of FLIRE data to the expected conditions in a different system. To this end, the experimental data was compared to a simple analytical model. The model is "simple" due to the inert and insoluble nature of helium in lithium and the assumptions used to find an analytical solution. The assumptions of the model are the following:

- one dimensional diffusion from bulk to surface;
- semi-infinite domain;
- all ions are implanted at the mean range *r*;
- the size of the beam is much smaller than the width of the channel; and
- convective transport is neglected.

With these assumptions, the governing partial differential equation (PDE) is

$$v\frac{\partial C}{\partial y} = D\frac{\partial^2 C}{\partial x^2} + G(x, y). \tag{9}$$

The boundary conditions are the following:

$$\begin{aligned} &C(x = 0, y) = 0,\\ &C(x = \infty, y) = 0,\\ &C(y = 0, x) = 0,\\ &G(x, y) = \tfrac{\phi}{W}\delta(x - r)\delta(y). \end{aligned} \tag{10}$$

In Eqs. (9) and (10), v is the flow speed, C the concentration of helium in the lithium, D is the diffusion coefficient for helium in lithium, G the helium source rate density due to implantation, ϕ is the total injection rate into the flow, r the mean implantation range, W the width of the ramp, x the distance into the depth of the flow and y is the distance along the ramp. The origin is located where the center of the ion beam intercepts the surface of the liquid. Using the analytical solution of the PDE, the rate at which particles flow into the lower chamber, q, can be written as [28,29]:

$$q = \phi\,\mathrm{erf}\left[\left(4\frac{Dy_0}{vr^2}\right)^{-1/2}\right] = \phi\,\mathrm{erf}\sqrt{\theta}, \tag{11}$$

where θ is a dimensionless parameter given by

$$\theta = \frac{vr^2}{4Dy_0} = \frac{r^2}{4Dt_\mathrm{I}} = \frac{t_\mathrm{D}}{t_\mathrm{R}}. \tag{12}$$

The retention coefficient is then given by:

$$R = \frac{q}{j} = \mathrm{erf}(\theta). \tag{13}$$

This result is consistent with expressions found in the literature for similar models [30–32]. In the above relations, y_o is the distance along the ramp to the exit channel, t_R is the residence time of the flow in the implantation chamber and t_D is the diffusion time. Expressions different from Eq. (13) can be obtained if the implantation source term is modified in the model to

allow for realistic particle implantation depth profiles, and/or spatial flux distribution along the travel path of the flow.

Because retention is defined as the release rate divided by the injection rate (Eq. (13)) indicates that the retention coefficient should be independent of the ion injection rate ϕ, as was shown from the experimental results. For small values of the argument, the error function is a linear function of the argument given by:

$$\mathrm{erf}(x) \approx 1.114x, \quad \text{for } x \ll 1. \tag{14}$$

This means that the retention coefficient R depends on energy and velocity in the following way if all other parameters are kept constant:

$$R \propto \frac{E}{\sqrt{v}}. \tag{15}$$

This dependence was confirmed from the experimental data shown in Figs. 17 and 18. From these retention results, the value of θ as a function of energy is given by:

$$\theta = (2.26 \times 10^{-5}\,\mathrm{keV}^{-2})E^2. \tag{16}$$

This means that if the transit time in the reactor and liquid temperature are on the same order, the retention value can be extrapolated to higher energies, since the edge temperature is expected to increase for low-recycling walls.

4. Summary of ion-beam sputtering yield measurements from liquid-metals in IIAX

One key feature in liquid-metal sputtering measurements in IIAX is that there is little difference between sputtering from a solid and liquid at temperatures just above the melting temperature of the liquid-metal. This behavior is also noted in results from PISCES-B. This implies that simply a change in phase does not lead to a measurable difference in sputtering.

Studies of lithium in the solid state with surface treatment using deuterium plasmas led to an average 40–60% decrease in lithium sputtering compared to results from a pure lithium target [7,8,20,33]. This result was also found for lithium in the liquid-state just above its melting point. The preferential sputtering of implanted D atoms from the lithium surface dilutes the partial sputtering yield of lithium, thus the measured decrease in lithium sputtering. This effect became less dominant as the temperature of the liquid-metal was increased due to the high diffusivity of implanted D atoms in liquid lithium. How implanted D atoms dilute the partial sputtering yield of lithium remains unresolved.

In addition to the effect of D-treatment of liquid lithium on the sputtering of lithium, the ion-bombardment-induced secondary sputtered ion fraction (IISSIF) was measured to be between 55–70%. This result was obtained for solid and liquid lithium with solid lithium having an IISSIF of about 55% and liquid lithium having an IISSIF at 420 °C of 70%. The result of the IISSIF in the solid state was confirmed later by tokamak experiments using the DiMES sample system in DIII-D. Solid lithium results from bombardment by D plasma showed agreement with neutral lithium sputtering yields assuming an IISSIF near 65%. Liquid lithium IISSIF results were confirmed by tokamak experiments in the T11-M TRINITI liquid lithium capillary divertor system.

Studies with 0.8 Sn–Li alloy in IIAX at temperatures at or just above the melting temperature (320 °C), showed lithium sputtering yields larger than pure liquid lithium. In addition, the secondary sputtered ion fraction was close to 65–70% indicating that 0.8 Sn–Li may be an attractive plasma-facing component for future high-heat flux fusion devices. The desirable low Z and high ion fraction of the sputtered flux is present due to the Li segregating to the surface. However, the disadvantages of a Li surface – high evaporation rate, low boiling point, and high tritium retention – are absent.

In turn, studies with liquid-phase tin showed lower tin sputtering yield than oxidized tin in the solid state. This was due to the unique behavior of tin-oxide sputtering more than its pure metal state. Moreover, just above the melting point of tin the sputtering yield did not change from oxygen-free tin in the solid state. This result was consistent with measurements for liquid lithium and liquid tin–lithium.

As the temperature was increased for all liquid-metals studied in IIAX and those in PISCES-B, a nonlinear rise in sputtering was measured. In the case of IIAX liquid-metal data, the rate of nonlinear erosion with temperature was relatively lower than measurements in PISCES-B, although one should take caution in comparison between the sets of data since the setup

of the two experiments are quite different. IIAX uses an ion-beam source at oblique incidence with an average flux of 10^{14} ions/(cm^2 s), whilst PISCES-B is a linear plasma source of flux near 10^{18} ions/(cm^2 s) with bombarding ions at normal incidence. Continued studies are determining the physical mechanisms responsible for the measured enhancement and difference/similarities between experiments in IIAX and PISCES-B.

5. Summary of particle retention measurements in FLIRE

Studies of retention of implanted He^+ ions in free-surface flowing liquid lithium have been completed in FLIRE. Measurement of particle retention is accomplished by implanting particles in a flowing lithium stream in the FLIRE upper chamber and measuring particle release in the lower chamber. The lower chamber is vacuum isolated from the upper chamber by the flowing lithium stream. Knowing the implantation rate and location, along with the lower-chamber pump speed and helium/hydrogen partial pressure, allows the calculation of the retention coefficient for bombarding helium or hydrogen ions.

Measurements of helium retention were performed as a function of incident particle energy and flow velocity to corroborate the qualitative behavior of the retention coefficient. As expected, retention is independent of incident particle flux, since the release measured adjusts to the increase in ion current in a proportional fashion. The retention coefficient increases linearly from 0.25% for 500 eV particles to 2% for 4 keV particles when the flow velocity is 44 ± 7 cm/s and the path traveled by the film is 10 cm. Retention also increases in proportion to the square root of the flow speed, as predicted by the simple diffusion model. Use of this model, combined with the experimental retention measurements, allow for the extrapolation of this data to other operation regimes, such as particles implanted with higher energy or different residence time of the flow in the reactor, provided all other conditions (i.e., temperature and flux) are similar to those encountered in FLIRE. Even though the simple model presented here is adequate to describe the transport of particles implanted by a beam source, more complete models would be needed if other irradiation conditions exist, in order to obtain an appropriate relationship between the retention coefficient R and the dimensionless parameter.

Current experiments are addressing the long-term retention of helium and the absorption and transport of hydrogen isotopes using both prompt release and TDS measurements. Once the flowing liquid lithium campaign is completed, experiments with liquid gallium or tin will commence. Gallium and tin offer the experimental advantage of easier handling (few corrosion issues), and gallium does not require as high an operating temperature as lithium.

Acknowledgements

The authors would like to thank the talented and valuable work of our undergraduates involved in the last three years of liquid-metal work at the University of Illinois at Urbana-Champaign: Matt Hendricks, Mark Boaz, Leslie Manohar, Marya Lazebnik, Sarfraz Taj, Daniel Rokusek, Ernesto Vargas-Lopez, Gabriel Burt, Jason Tillery, Donna Carpenter, Wayne Lytle and Ian Treviranus. Also, graduate students: Darren Alman, Martin Neumann, Rajiv Ranjan and Jeffrey E. Norman. Valuable comments and discussions from: A. Hassanein, J. N. Brooks, P. Sigmund, R. Bastasz, R. Doerner, D. Whyte, S. Mirnov, I. Konkashbaev, S. Krasheninnikov and M. Baldwin are acknowledged. This work was supported by the U.S. Department of Energy ALPS (Advanced Limiter/divertor Plasma-facing Surfaces) Grant # DE-FG02-99ER54515.

References

[1] M.F. Dumke, T.A. Tombrello, R.A. Weller, R.M. Housley, E.H. Cirlin, Surf. Sci. 124 (1983) 407.
[2] T.B. Lill, W.F. Callaway, M.J. Pellin, D.M. Gruen, Phys. Rev. Lett. 73 (12) (1994) 1719.
[3] R.W. Conn, R.P. Doerner, F.C. Sze, S. Luckhardt, A. Liebscher, R. Seraydarian, D.G. Whyte, Nucl. Fusion 42 (2002) 1060.
[4] R.P. Doerner, M.J. Baldwin, R.W. Conn, A.A. Grossman, S.C. Luckhardt, R. Seraydarian, G.R. Tynan, D.G. Whyte, J. Nucl. Mater. 290–293 (2001) 166.
[5] R.P. Doerner, M.J. Baldwin, S.I. Krasheninnikov, D.G. Whyte, J. Nucl. Mater. 313–316 (2003) 385.
[6] J.P. Allain, Master Thesis, University of Illinois-Urbana-Champaign, 2000.
[7] J.P. Allain, D.N. Ruzic, Nucl. Fusion 42 (2002) 202.
[8] J.P. Allain, Ph.D. Thesis, University of Illinois-Urbana-Champaign, 2001.

[9] J.P. Allain, D.N. Ruzic, M.R. Hendricks, J. Nucl. Mater. 290–293 (2001) 180.
[10] J.P. Allain, D.N. Ruzic, M.R. Hendricks, J. Nucl. Mater. 290–293 (2001) 33.
[11] P.C. Smith, D.N. Ruzic, Nucl. Fusion 38 (5) (1998) 673.
[12] A.B. Dewald, A.W. Bailey, J.N. Brooks, Phys. Fluids 30 (1) (1987) 267.
[13] J.N. Brooks, Phys. Fluids B-Plasma Phys. 2 (8) (1990) 1858.
[14] P.C. Stangeby, The Plasma Boundary of Magnetic Fusion Devices, Institute of Physics Publishing, Bristol, 2000.
[15] J.P. Allain, D.A. Alman, Z. Insepov, J.N. Brooks, L.E. Gonzalez, J. Nucl. Mater. (2003), submitted for publication.
[16] J. P. Allain, M. D. Coventry, D.N. Ruzic, J. Appl. Phys. (2003), submitted for publication.
[17] M.D. Coventry, J.P. Allain, D.N. Ruzic, J. Nucl. Mater. 313–316 (2003) 640.
[18] R. Bastasz, W. Eckstein, J. Nucl. Mater. 290–293 (2001) 19.
[19] A.R. Krauss, D.M. Gruen, J. Nucl. Mater. 85 & 86 (1979) 1179.
[20] J.P. Allain, D.N. Ruzic, in: A. Hassanein (Ed.), NATO Science Series: Hydrogen and Helium Recycling at Plasma Facing Materials, vol. 54, Kluwer Academic Publishers, Dordrecht, 2002, p. 73.
[21] J.P. Allain, D.N. Ruzic, M.D. Coventry, D.A. Alman, M. Nieto, Phys. Rev. Lett., (2003), submitted for publication.
[22] M.A. Abdou, R.F. Mattas, APEX Interim Report, UCLA-FNT-1072, 1999.
[23] R. Kelly, N.Q. Lam, Radiat. Effects 19 (1) (1973) 39.
[24] M.D. Coventry, J.P. Allain, D.N. Ruzic, J. Nucl. Mater. (2003), submitted for publication.
[25] M.J. Baldwin, R.P. Doerner, S.C. Luckhardt, R. Seraydarian, D.G. Whyte, R.W. Conn, Fusion Eng. Des. 61–62 (2002) 231.
[26] M.J. Baldwin, R.P. Doerner, R. Causey, S.C. Luckhardt, R.W. Conn, J. Nucl. Mater. 306 (2002) 15.
[27] J.P. Allain, M. Nieto, M.D. Coventry, M.J. Neumann, E. Vargas-Lopez, D.N. Ruzic, Fusion Eng. Des. 61–62 (2002) 245.
[28] M. Nieto, J.P. Allain, M.D. Coventry, E. Vargas-Lopez, D.N. Ruzic, J. Nucl. Mater. 313–316 (2003) 646.
[29] M. Nieto, D.N. Ruzic, J.P. Allain, Fusion Sci. Technol. 44 (1) (2003) 232.
[30] C. Liao, M.S. Kazimi, J.E. Meyer, Fus. Technol. 23 (1993) 208.
[31] A. Hassanein, J. Nucl. Mater 302 (2002) 41.
[32] A. Hassanein, I. Konkashbaev, J. Nucl. Mater 273 (1999) 326.
[33] J. László, W. Eckstein, J. Nucl. Mater 184 (1991) 22.